AIAA SciTech Forum
8-12 January 2024, Orlando, FL
AIAA SCITECH 2024 Forum

10.2514/6.2024-2380

Computational Analysis of Secondary Droplet Breakup at Transcritical Conditions with Surface Tension Effects

Prajesh Jangale[1]
J. Mike Walker '66 Mechanical Engineering Department, Texas A&M University, College Station, TX 77843, USA

Bradley Boyd[2]
Department of Mechanical Engineering, University of Canterbury, Private Bag 4800, Christchurch 8140, New Zealand

Dorrin Jarrahbashi[3]
J. Mike Walker '66 Mechanical Engineering Department, Texas A&M University, College Station, TX 77843, USA

In the pursuit of enhanced engine performance and reduced emissions, the design of liquid-fueled propulsion systems is shifting towards much higher combustor pressures, surpassing the nominal critical pressure of the fuel and air. This trend leads to the adoption of supercritical conditions, wherein the liquid fuel is injected into the ambient air at supercritical pressure and temperature, causing the fuel temperature to exceed its nominal critical point. This transition from a liquid-like to a gas-like behavior, known as "transcritical behavior," is a crucial aspect governing the operation of modern high-pressure propulsion and energy conversion systems. In these systems, the primary liquid jet breakup and the subsequent breakup of the resulting droplets into smaller droplets, namely secondary breakup, significantly impact mixing and combustion processes. Despite its importance, there has been a limited focus on droplet breakup at supercritical conditions, particularly at higher flow speeds relevant to high-speed liquid-fuel propulsion systems. Surface tension effects are often neglected in the simulation of transcritical flow, assuming surface tension vanishes beyond the critical point, while recent experiments and molecular dynamics simulations suggest that surface tension effects persist at transcritical conditions. To gain insight into the effects of surface tension on transcritical flows, we have developed a fully compressible multiphase Direct Numerical Simulation (DNS) approach that accounts for decaying surface effects. The diffuse interface method is employed to represent transcritical interfaces, accounting for surface tension effects calculated using molecular dynamics simulations. This approach is employed to investigate the behavior of subcritical n-dodecane droplets in a supercritical nitrogen environment interacting with a shockwave, aiming to identify the governing breakup regimes at transcritical conditions. The development of quantitative measures enables the generalization of droplet breakup modes for transcritical droplets. The insights gained from this study contribute to advancing the understanding of transcritical liquid breakup, providing valuable knowledge for designing and optimizing high-speed propulsion systems.

[1] PhD Candidate, Mechanical Engineering, AIAA Student Member
[2] Postdoctoral Researcher, Mechanical Engineering
[3] Assistant Professor, Mechanical Engineering, AIAA Member

I. Background

The design of heavy liquid hydrocarbon-like n-dodecane fuel propulsion systems is shifting toward much high speed and high-pressure applications [1-3]. In these propulsion systems, the combustor pressures exceed the nominal critical pressure of the fuel and air to enhance engine performance and lower emissions [1, 2, 4]. For high-speed liquid-fueled propulsion systems, shockwave interacts with fuel droplets inside the combustion chamber, increasing the challenges in understanding liquid fuel secondary breakup, evaporation, and atomization at supercritical conditions, which determine the fuel-air mixing and combustion outcomes. A subcritical liquid fuel is injected into the ambient air at supercritical pressure and temperature, gradually increasing the fuel temperature to exceed its nominal critical point. The transition of a denser liquid-like fuel at subcritical temperature into a gas-like fluid at supercritical temperature by crossing the pseudo-boiling line is referred to as "transcritical behavior" [5, 6]. Breakup and mixing of fuel droplets significantly differ at subcritical and transcritical conditions [7-10].

Shock-driven droplet breakup, known as aerobreakup, has been extensively studied at near-atmospheric and isothermal conditions; however, aerobreakup behavior and breakup morphology (modes) at supercritical conditions have remained elusive. There are several computational studies of shock-droplet interaction using sharp-interface and diffuse-interface approaches at subcritical conditions [11-16]. The breakup regime diagrams have been traditionally identified for water droplets at subcritical conditions [14, 17-22]. However, there are only two reports that simulate the fuel droplet-shock interaction at transcritical conditions [23, 24]. In our previous work [24], we revealed the shock dynamics in the interaction of a shockwave with an n-dodecane droplet at near-critical conditions. In this study, we investigate different droplet breakup regimes at transcritical conditions under the influence of surface tension effects. The role of surface tension is typically neglected in transcritical flow simulations [18, 25-36]. However, it has been shown theoretically [3] that the surface tension between fuel and air persists even at supercritical pressures. Experimental results have shown that droplets are present at transcritical conditions after the end of injection in a high-pressure combustor, indicating the persistence of surface tension even at supercritical pressure and temperature with respect to the nominal critical point of the fuel [37]. These experiments [37] also indicated that it takes a few milliseconds for a microscopic droplet exposed to supercritical conditions to be heated to the critical temperature. The droplet then turns into a gas-like fluid with no surface tension effect that diffuses into the background supercritical environment, referred to as supercritical gas-like diffusion. With an increase in interface temperature, the interface diffuses, and the surface tension decays. The surface tension decay dictates the transition from subcritical to supercritical conditions. Due to the lack of experimental data on surface tension decay, MD results are used in this study to replicate the effects of surface tension changes on breakup. To this end, the interfacial behavior of an n-dodecane droplet surrounded by pressurized nitrogen is delineated using molecular dynamics simulations (MD) [38]. MD simulations [38] have shown that during the transition from subcritical to supercritical conditions, surface tension gradually decays to zero, and surface tension decay rate can dictate the onset of transition from a classical two-phase breakup regime to a gas-like diffusion regime that occurs in the absence of surface tension effects. The transition unfolds in three distinct stages. Initially, during the transcritical phase, the interface undergoes thickening, and surface tension experiences decay, primarily influenced by surface evaporation. Subsequently, the undroplet phase ensues, characterized by a zero-surface tension, as the droplet's core transforms from a liquid-like to a gas-like state, and the droplet core becomes disintegrated as the background nitrogen diffuses into the droplet core. Finally, the diffusion phase emerges, marked by the mixing of two gas-like fluids at supercritical temperatures [38]. During the transcritical phase, the surface tension coefficient exhibits a time-dependent decay influenced by temperature, pressure, and droplet size. However, normalizing the time relative to the undroplet timescale enables the scaling-up of the surface tension decay rate from nanoscale molecular simulations to microscale continuum simulations. This normalization renders the coefficient independent of droplet size [38].

Subcritical droplet aerobreakup, studied in shocktubes and wind tunnels, depends on the Weber (We) and Ohnesorge (Oh) numbers defined as $We = \frac{\rho_g u_g^2 d_0}{\sigma}$, where ρ_g, u_g are the post-shock density and velocity, d_0 is the droplet initial diameter, and σ is the surface tension coefficient; and $Oh = \frac{\mu_l}{\sqrt{\rho_g \sigma d_0}}$, considers the effects of droplet viscosity (μ_l) and surface tension. Several studies have identified five breakup mechanisms as follows: vibrational breakup, bag breakup, bag-and-stamen breakup, sheet stripping, and wave crest stripping, leading to catastrophic breakup [39, 40]. The breakup modes are distinguished based on the critical Weber number (We), representing the balance between inertial and surface tension forces [41, 42]. For low Ohnesorge numbers (Oh < 0.1), the vibrational mode occurs for We < 12 and bag breakup occurs for 12 < We < 50. The breakup mode transitions to the bag-and-stamen breakup mode for 50 < We < 100, and the sheet-stripping mode is observed for 100 < We < 350, followed by catastrophic breakup detected for We > 350 [43]. More recently, the aerobreakup modes are categorized into two regimes: Rayleigh–Taylor piercing (RTP) identified for 10 < We < 10^2 evolving into multi-wave piercing, and shear-

induced entrainment (SIE) dominating for We > 10^3 [44, 45]. This categorization provides insights into breakup mechanisms within rarefied and supersonic gas flows. However, a gap exists in understanding how the identified breakup modes for subcritical conditions apply to transcritical conditions. In this study, the breakup behavior of an n-dodecane droplet initially at a subcritical temperature (363 K) impacted by a shockwave in a supercritical nitrogen environment with respect to the n-dodecane nominal critical point (658 K, 1.82 MPa), representing the transcritical conditions is studied. We consider the influence of surface tension effects on droplet breakup behavior at transcritical conditions for a wide range of density ratios. Our MD simulations provide the variation of surface tension coefficients for n-dodecane for a range of nitrogen pressures and temperatures. For the purpose of this study, we assume that the surface tension decays and reaches zero in a finite time period during the simulations, according to our MD simulation results [38].

II. Computational Methodology

The breakup of an isolated droplet interacting with a normal shockwave in a supercritical environment is simulated using a Direct Numerical Simulation (DNS) approach following a Diffuse-Interface method (DIM). In this study, we focus on the effects of surface tension and neglect the molecular diffusion, heat conduction, and viscous effects. Implementing the surface tension force into the governing equations using a 5-equation model aligns with the methodology introduced by Garrick et al. [13]. The surface tension coefficient has been calculated using MD-based models developed for transcritical conditions, as detailed in Section III.B. A decaying surface tension coefficient has also been applied based on the normalized molecular dynamics model. We consider a compressible, inviscid, multiphase model following the governing equations (1-5) for a diffuse-interface two-species system as follows: two continuity equations (1-2), momentum (3), and energy (4) equations for the mixture and the volume fraction advection equation (5).

$$\frac{\partial(\alpha_D\rho_D)}{\partial t} + \nabla\cdot(\alpha_D\rho_D\boldsymbol{u}) = 0, \tag{1}$$

$$\frac{\partial(\alpha_S\rho_S)}{\partial t} + \nabla\cdot(\alpha_S\rho_S\boldsymbol{u}) = 0, \tag{2}$$

$$\frac{\partial(\rho\boldsymbol{u})}{\partial t} + \nabla\cdot(\rho\boldsymbol{u}\otimes\boldsymbol{u} + p\boldsymbol{I}) = -\sigma\kappa\nabla\alpha_D, \tag{3}$$

$$\frac{\partial E}{\partial t} + \nabla\cdot\big(\boldsymbol{u}(E+p)\big) = -\sigma\kappa\boldsymbol{u}\cdot\nabla\alpha_D, \tag{4}$$

$$\frac{\partial\alpha_D}{\partial t} + \boldsymbol{u}\cdot\nabla(\alpha_D) = 0, \tag{5}$$

where α_D is the volume fraction, ρ is the density, $\boldsymbol{u}$ is the velocity vector, p is the pressure, E is the total energy $E = \rho\left(e + \frac{|\boldsymbol{u}|^2}{2}\right)$, e is the internal energy, σ is the surface tension coefficient, κ is the local interface curvature, and $\boldsymbol{I}$ is the identity matrix. The mass fraction of the second species of the two-component system (D and S representing the droplet and the surrounding fluids, respectively) is characterized by defining a mixture rule as $\alpha_S = 1 - \alpha_D$. The system of equations, Eqs. (1-5) is closed using the stiffened gas equation of state (EoS) given by Eq. (6).

$$\Gamma p + \Pi = E - \frac{1}{2}\rho|\boldsymbol{u}|^2, \tag{6}$$

where $\Gamma = \frac{1}{\gamma-1}$, $\Pi = \frac{\gamma\pi_\infty}{\gamma-1}$, γ, and π_∞ are properties of the fluids.

The stiffened equation of state is used in this study due to its simplicity, computational efficiency, and stability compared to the Peng-Robinson EoS. Given that the tested conditions are sufficiently distant from the critical point (Table 1), which is known to induce spurious pressure oscillations, the utilization of a more sophisticated Equation of State (EoS) and mixture rules, such as Peng-Robinson as implemented in our prior investigation, is unnecessary [24, 46]. To this end, the stiffened gas EoS is chosen for this study to effectively capture the overarching breakup behavior under the current conditions. This study uses DIMP-CFD code, which is an in-house, density-based, finite volume solver in C++ parallelized using domain decomposition and message passing interface (MPI). The details of the solver and validation cases against the multicomponent shocktube problem and droplet-shock interaction are discussed in Ref. [24]. The temporal discretization uses the third-order total-variation-diminishing Runge–Kutta scheme (RK3-TVD) [47] with a Courant-Friedrichs-Lewy (CFL) condition equal to 0.8. The Harten–Lax–van Leer-contact (HLLC) approximate Riemann flux is used to determine the Godunov flux at the cell interfaces [48-50]. An artificial interface smoothening method following the method discussed in our previous work [50] is employed to reduce the spurious pressure oscillations near the critical point. As the droplet is defined on a uniform Cartesian mesh, this interfacial thickening helps with creating a smooth curvature for the initial droplet shape. The Monotone Upwind Schemes for

Conservation Laws (MUSCL) and the Tangent of Hyperbola for Interface Capturing (ρ-THINC) method are employed as presented in Ref. [16]. The interface shape parameter for the THINC method is set to $\beta = 1$, which is consistent with the initial interface smoothing function. The surface tension terms are included in the momentum and energy equations (Eqs. 3-4) [13, 51]. Additionally, the HLLC flux is modified to include the pressure jump due to the capillary force following the procedure outlined in Ref. [13]. The local interface curvature is determined using the interface normal, which is described as a function of the mass fraction given in Eq. (7).

$$\kappa = -\nabla \cdot \boldsymbol{n} = -\nabla \cdot \left(\frac{\nabla \alpha_D}{|\nabla \alpha_D|}\right). \tag{7}$$

The curvature calculation procedure, as described in Garrick et al. [13], involves computing the normal vector using fourth-order central difference. Subsequently, curvature is determined from the normal vector using second-order central difference. Finally, the curvature is extended outwards from the interface center ($\alpha_D = 0.5$) using ten iterations of the filtering procedure [13]. The validation of the surface tension model adopted in this study is discussed below. The oscillation of an initially ellipsoidal droplet in $[x, y]$ domain described by Eq. (8) [51] is considered:

$$\frac{(x-0.5)^2}{a^2} + \frac{(y-0.5)^2}{b^2} = 1, \tag{8}$$

where $a = 2$ and $b = 1.2$. The computational domain $\Omega = [0,1] \times [0,1]$ with a 200×200 mesh cell, and a CFL number equal to 0.8 is used. The liquid density is $\rho_l = 100\ \mathrm{kg/m^3}$, and the surrounding gas density is $\rho_g = 1\ \mathrm{kg/m^3}$. The theoretical period (T_p) of oscillation can be computed as

$$T_p = 2\pi\sqrt{\frac{(\rho_l+\rho_g)R^3}{6\sigma}}, \tag{9}$$

where $R = \sqrt{ab}$ is the equivalent circular radius. The surface tension coefficient is set as a constant to $\sigma = 350\ \mathrm{Pa} \cdot s$, resulting in $T_p = 0.084\ \mathrm{s}$. Fig. 1 gives the variation of the global kinetic energy corresponding to the droplet oscillation, which validates the effect of surface tension.

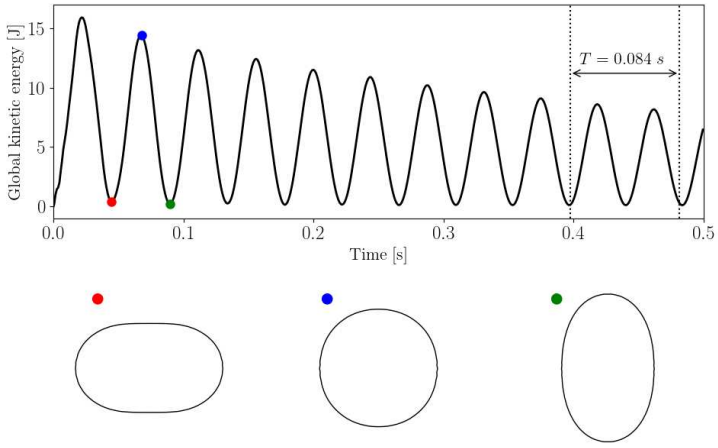

Figure 1. Global kinetic energy corresponds to the oscillations of a droplet to validate the surface tension model, as represented in Ref [51].

III. Computational Model

A. Droplet-shock Interaction DNS Setup

A normal shockwave travels from left to right, impacting an n-dodecane droplet with an initial droplet diameter of d_0 =50 μm as shown in Fig. 2. The incident shockwave, initially at z = -150 μm, is introduced as a discontinuity in fluid properties. The computational domain is extended to [-$8d_0$, $8d_0$] in the streamwise direction and [-$4d_0$, $4d_0$] in the spanwise direction. The size of the computational domain is sufficiently large to avoid the possible interaction of erroneous reflections from the non-reflective boundaries with the droplet throughout the simulation. The computational domain consists of a uniform mesh in the region [-$6d_0$, $6d_0$] and from the axis of symmetry to the region [-$3d_0$, $3d_0$] to increase the computational speed. 1200 nodes in the inner uniform region in the z-direction and

600 nodes in the r-direction are considered. The mesh size is chosen to ensure 100 cells are included within the droplet diameter to ensure the droplet breakup is resolved as suggested in previous simulations of aerobreakup [14]. At r = 0, a symmetric boundary condition is imposed, allowing the simulation of only half of the domain. To expedite the simulations, the results from the upper half are mirrored onto the lower half. A transmissive boundary condition is implemented at the left, right, and outer boundaries. The velocity component in the z-direction is denoted by u_z and the initial velocity in the r-direction (u_r) is zero everywhere.

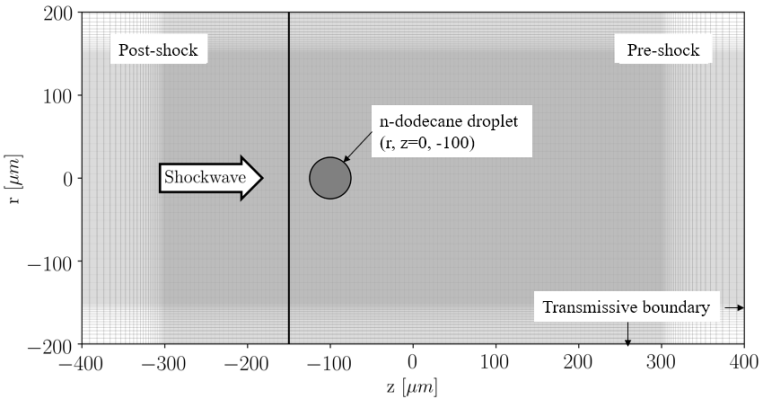

Figure 2. The computational setup for the shock-droplet interaction shows the grid and boundary conditions. The grid has been enlarged in this figure. The actual mesh density is twice as given in the figure.

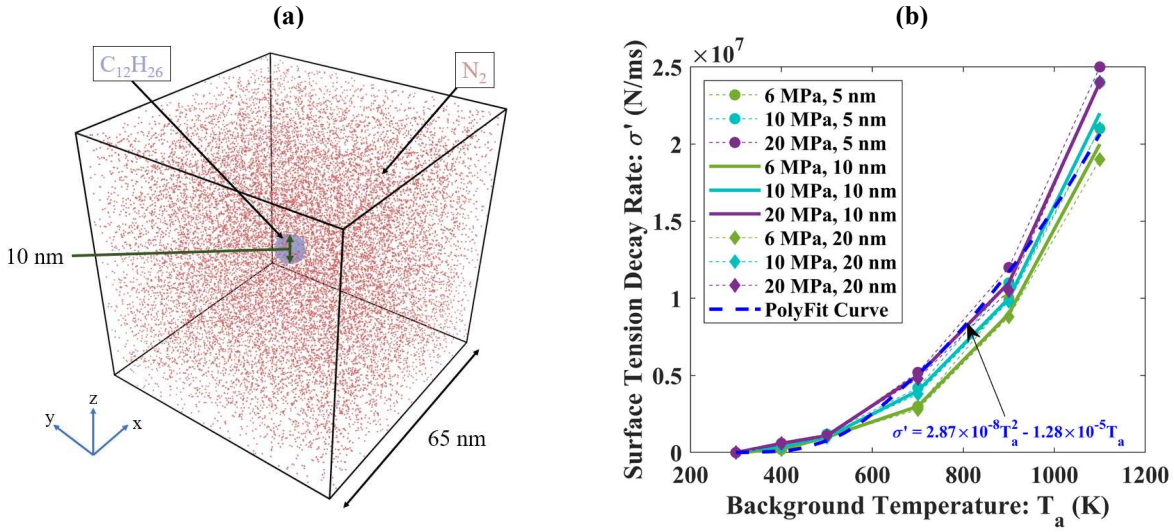

Figure 3. (a) Simulation setup showing nitrogen and n-dodecane molecules as marked. (b) Surface tension decay rate variation with the nitrogen background temperature for different nitrogen pressure and *n*-dodecane droplet size along with a polyfit curve as a function of background temperature.

B. Molecular Dynamics Simulation Model

For the surface tension calculation, MD simulation is set up with 6-9 Lennard-Jones potential function $\varphi(r)$ for molecular interactions given by Eq. (10), where ϵ is the depth of the potential well, l is the finite distance at which the inter-particle potential is zero, and r indicates the distance between the atoms. A large-scale atomic/molecular massively parallel simulator (LAMMPS) [52] software is used for running the simulation with a sample case setup shown in Fig. 3a. The n-dodecane droplet diameter varies from 2 to 20 nm, and the simulation box with surrounding nitrogen molecules is a cube of 65 nm with periodic boundary condition on all sides. The equilibration run is performed with an NPT ensemble (N-number of molecules, P-pressure, and T-temperature are conserved) to apply the initial condition, which is n-dodecane molecules at 363 K temperature and nitrogen molecules at 900 K temperature and 6

MPa pressure. The main simulation is run with an NVE ensemble (N-number of molecules, V-volume, E-energy) with a timestep of 2 fs for a simulation time of 2 ns. The surface tension decay with time for the binary fluid system is calculated using the Irving-Kirkwood method [53] based on the pressure tensor given in Eq. (11). The local normal and tangential components of pressure tensor, i.e., $p_N(k)$ and $p_T(k)$, respectively, are calculated in k's slab within the computational domain where $k = 1, \dots, N_s$. More details on the setup and calculations are given in Ref. [38]. A range of simulations is performed with variations in droplet size from 2-20 nm, background temperature from 300-1100 K, and background pressure from 1-20 MPa. The decay of surface tension occurs over a finite duration and is normalized by the undroplet time, characterized as the time at which the droplet core is fully disintegrated, and gas-like n-dodecane and nitrogen undergo diffusion mixing. The surface tension decay rate shown in Fig. 3b is independent of background pressure and droplet size, allowing us to scale-up the data obtained from the MD using multiple regression and gradient tree-boosting data-driven models into continuum simulations. Fig. 3b also indicates that the decay rate increases with background temperature, which is due to increased molecular kinetic energy [38].

$$\varphi(r) = \epsilon\left(2\left(\frac{l}{r}\right)^9 - 3\left(\frac{l}{r}\right)^6\right) \tag{10}$$

$$\sigma = \frac{1}{2}\int_0^{N_s}\left(p_N(k) - p_T(k)\right)dk \tag{11}$$

IV. Results and Discussion

A. Simulation Parameter Space

Table 1 presents different simulation cases for a wide range of ambient temperatures (T_a) and pressures (P_a) for nitrogen above the nominal critical point for n-dodecane. n-Dodecane temperature (T_f) is kept constant at 363 K, which is below the critical point of n-dodecane. To this end, the conditions outlined in Table 1 represent transcritical conditions. The conditions chosen are relevant to high-pressure liquid-fuel injection experiments in a high-pressure vessel [37].

Table 1. Parameter space for simulation cases with density ratio, temperature, pressure, and surface tension calculated from MD simulations.

Case #	$\frac{\rho_g}{\rho_l}$	T_f (K)	T_a (K)	P_a (MPa)	σ_0 (N/m)
1	8	363	700	20	0.009
2	11	363	800	15	0.010
3	12	363	900	15	0.009
4	18	363	900	10	0.015
5	22	363	900	8	0.018
6	30	363	900	6	0.020
7	50	363	900	3.5	0.026
8	85	363	900	2	0.029
9	100	363	1100	2.1	0.018
10	130	363	1200	2	0.002

Variation of ambient nitrogen pressure and temperature leads to variation in density ratio ($\frac{\rho_g}{\rho_l}$) from 8 to 130. Therefore, density ratio is one of the crucial non-dimensional parameters governing the behavior of transcritical droplets. Other governing non-dimensional parameters include the Weber number and Ohnesorge number. The variation of surface tension with density ratio shown in Fig. 4a indicates a peak in surface tension coefficient at a density ratio equal to 85 and a decrease in surface tension coefficient past that density ratio. Variation of surface tension coefficient further affects We, as shown in Fig. 4a. By varying the post-shock speed from 5 to 50 m/s, a wide range of We is expected considering the changes in surface tension coefficient calculated using separate MD simulation for each case outlined in Table 1 as discussed in the previous section. For each flow speed, there is a minimum We at density ratio equal to 85. Variation of Oh with density ratio follows the same trend observed for We

with a minimum at density ratio equal to 85, as shown in Fig. 4b. It is noted that the droplet viscosity is calculated considering the nominal viscosity of n-dodecane at 363 K. The results shown here indicate that simultaneous variation of surface tension coefficient and density ratio lead to a wider range of We and Oh numbers for each flow speed, which are the crucial parameters governing the aerobreakup of transcritical droplets. This phenomenon is distinctive to transcritical droplets as for water droplets at subcritical conditions [43], various breakup modes are independent of density ratio, and the surface tension coefficient remains constant. Consequently, the breakup modes identified at subcritical conditions are mainly determined by Weber number, considering very low Ohnesorge numbers.

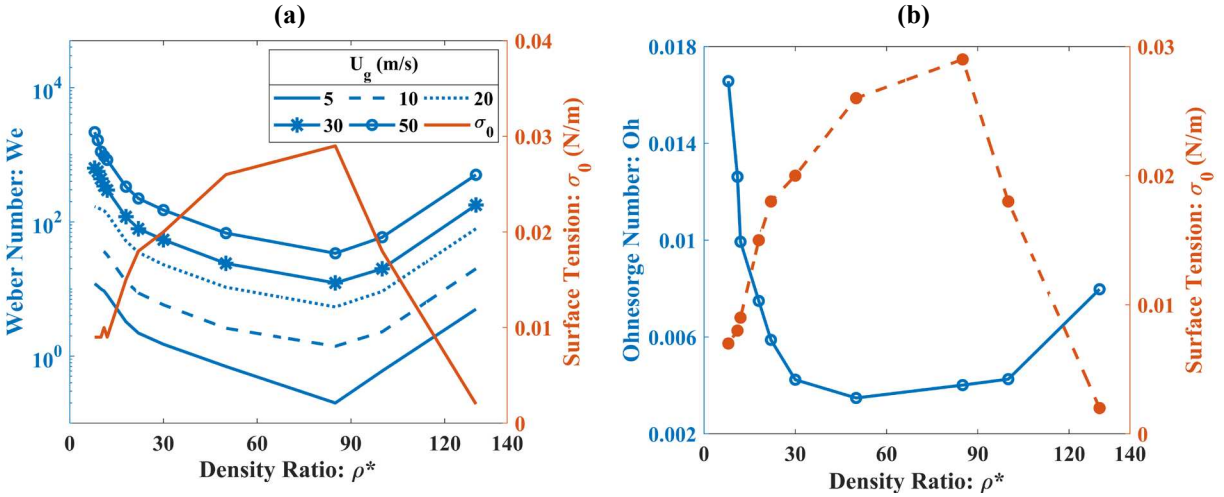

Figure 4. (a) Weber number variation with density ratio for varying post-shock flow speed (blue lines; (b) variation of Ohnesorge number with density ratio. The Secondary plot (orange line) shows the initial surface tension coefficient variation with density ratio.

B. Breakup Modes of Transcritical Droplets

The temporal development of the shock-driven droplet breakup modes for Case 8 outlined in Table 1 (900 K and 2 MPa temperature and pressure for the background nitrogen) for a wide range of post-shock flow speeds are shown in Fig. 5. The droplet size is 50 μm for all the cases. We considered Case 8 as it represents a density ratio equal to 85, at which a peak in surface tension coefficient is observed in Fig. 4. The Mach number varies from 1.01 to 1.07, resulting in a post-shock gas velocity varying from 10 to 70 m/s and *We* number varying from 1.2 to 70. The droplet morphologies portrayed by the maximum density contour are shown at different non-dimensional times defined based on the post-shock gas speed (u_g), density ratio ($\frac{\rho_g}{\rho_l}$), and the initial diameter of the droplet (d_0) as ($t^* = t\frac{u_g}{d_0}\sqrt{\frac{\rho_g}{\rho_l}}$). This non-dimensional time has been chosen to standardize the breakup behavior across all tested conditions. At lower Weber numbers, e.g., *We* =1.2, the droplet undergoes slight deformation and oscillations without breakup. At *We* = 5.4, the droplet undergoes a vibrational mode, exhibiting vertical deformation, ultimately returning to its circular shape (not shown here). At *We* =12, the droplet exhibits a crescent shape with two blobs of *n*-dodecane mass at the top and bottom of the deformed droplet that resembles a bag breakup mode, a common breakup mode identified subcritical droplets. With a further increase in *We* to 22, the droplet experiences a reverse (backward) bag formation with sheet thinning denoted by a thin ligament joining the two split blobs of liquid. The sheet thinning breakup mode is observed for *We* = 34. At *We* = 70, the droplet exhibits a more radially expanded shape, identified as whiplash [39] with sheet thinning, which is identified as thinning at the center and long fragmentation at the edges of the deformed droplet. The observed breakup modes exhibit distinctions from those witnessed in water droplets under subcritical conditions. Notably, in subcritical breakup scenarios, when compared to transcritical conditions at similar Weber numbers, subcritical droplets tend to undergo more pronounced vibrations before ultimate breakup. Additionally, a distinguishing feature is evident in the orientation of the bag-type breakup: in the subcritical breakup, the open portion of the bag is oriented in the direction of the flow (left to right in Fig. 5), referred to as forward bag [39], in contrast to the transcritical droplet breakup which exhibits a backward bag, i.e., the closed portion of the bag faces the flow from left to right [39]. To quantitatively identify the parameters differentiating the transcritical droplet breakup modes, we calculated the rate of growth of the droplet in normal and transversal directions for a range of *We* and density ratios,

as shown in Fig. 6a-b. The normal growth rate is calculated by measuring the speed of the droplet center of mass relative to the post-shock gas speed along the axial direction, non-dimensionalized with respect to the initial droplet diameter. The transversal growth rate is calculated as the rate of increase of droplet width perpendicular to the axis of symmetry, non-dimensionalized with respect to the initial droplet diameter. The highest range of growth rate variation is seen for the whiplash with sheet thinning mode which is expected as it has elongated fragments at the edges. The normal growth rate is similar for backward bag, forward bag, and backward bag with sheet thinning modes; however, these modes are differentiated using the transverse growth rate. The edges of the droplet are clearly pointed in opposite directions between forward and backward breakup. The backward bag with sheet thinning breakup exhibits a very small transverse growth rate as compared to regular sheet-thinning and whiplash with sheet-thinning modes. The vibrational breakup regime is characterized by a lower transverse growth rate compared to all other modes. Although the no-breakup mode is included for completeness, it exhibits no significant transverse growth rate. A very small normal growth rate, equivalent to the post-shock gas velocity, is identified for this particular case.

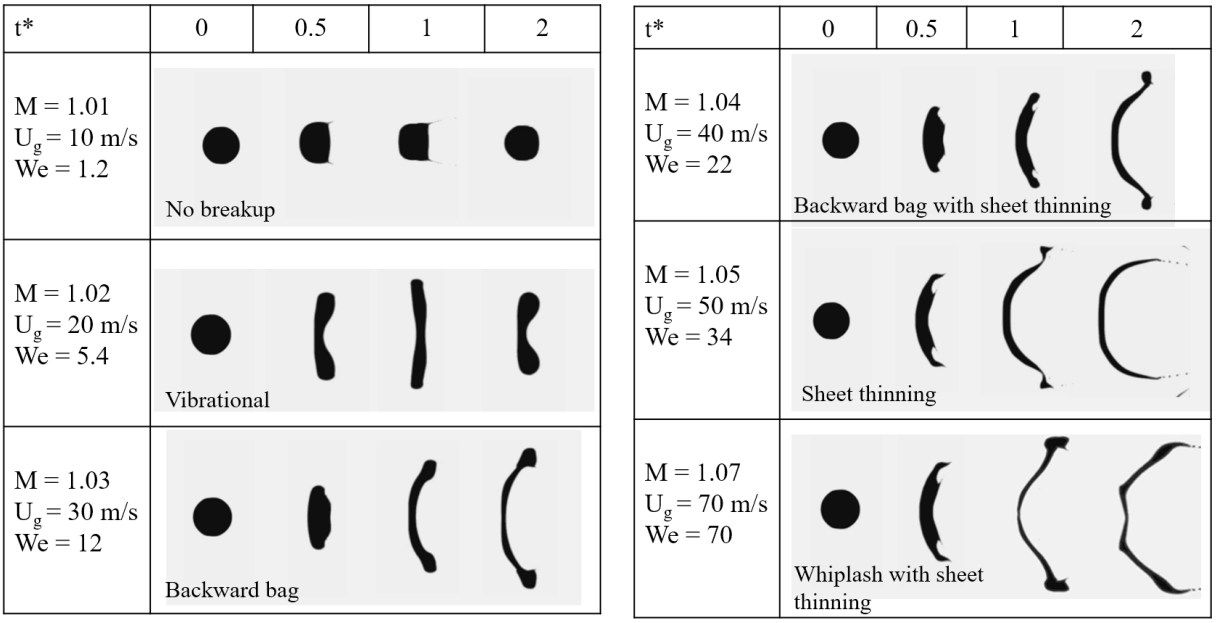

Figure 5. Transcritical droplet breakup modes by varying post-shock flow speeds at common non-dimensional times for Case 8 in Table 1, representing a density ratio of 85. The droplet morphology is captured using the density contours.

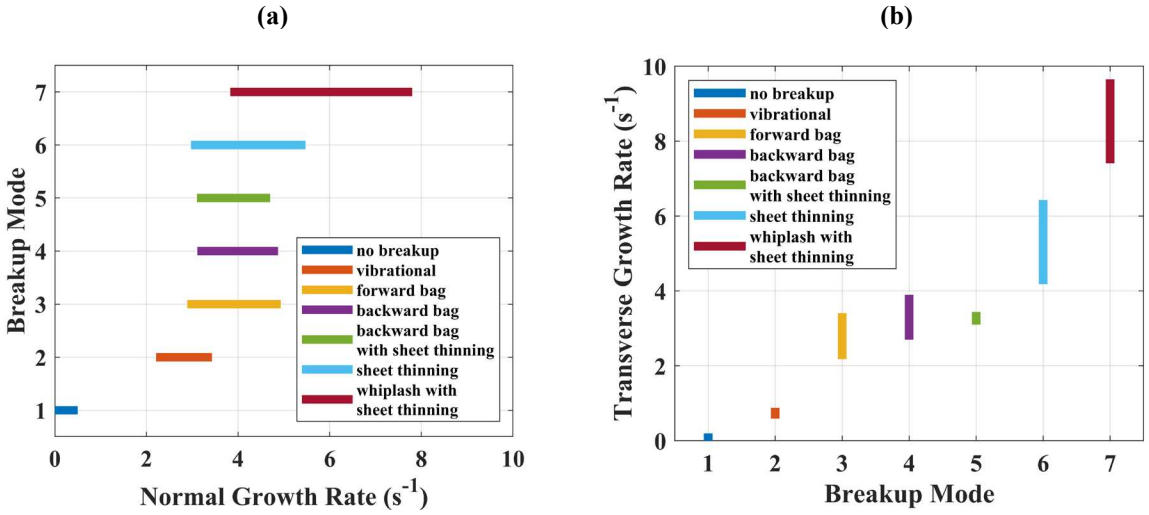

Figure 6. (a) Normal and (b) transverse growth rate for each of the transcritical breakup modes.

C. Variation of Surface Tension Coefficient

The surface tension coefficient is calculated from MD simulations for a droplet at subcritical temperatures exposed to a supercritical environment where both pressure and temperature exceed the critical point of the *n*-dodecane droplet as discussed in Section III.B. In the preceding section, a constant surface tension coefficient was assumed. However, in this section, we delve into the impact of surface tension variation over time on the breakup behavior of transcritical droplets when interacting with a normal shockwave. Initially, the surface tension coefficient for a *n*-dodecane droplet at 363 K surrounded by nitrogen is at 900 K temperature, and 6 MPa pressure is 20 mN/m based on MD simulations. These conditions are consistent with the Engine Combustion Network (ECN) standard Spray A conditions [54] that represent a transcritical spray as the droplet is initially at a subcritical temperature while the surrounding gas is supercritical with the temperature and pressure above the critical point of pure *n*-dodecane. We varied the surface tension coefficient linearly with time following the straight lines shown in Fig. 7. The slopes have been carefully chosen to ensure that the surface tension does not decay to zero throughout the breakup process. This allows us to capture how variations in the surface tension coefficient with time, as reflected in the transient Weber number, influence the breakup morphology of transcritical droplets.

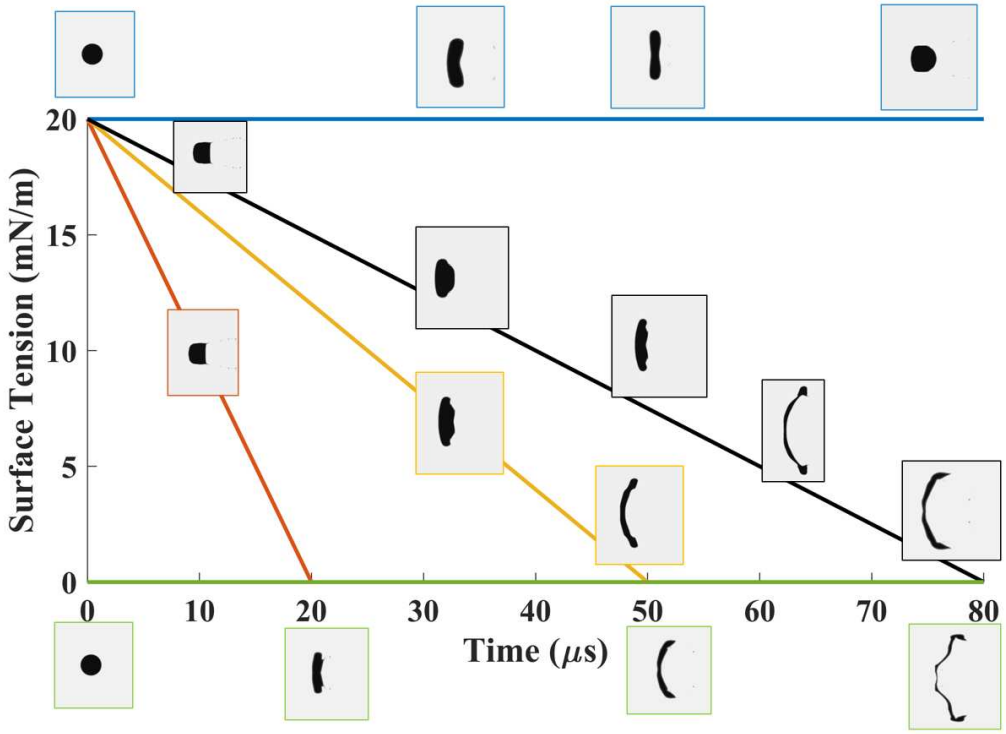

Figure 7. Different surface tension decay rates result in different breakup behavior.

Five different scenarios are considered here: zero surface tension (green line), constant surface tension (blue line), and three different decay rates (black, yellow, and red – in order of increasing the rate of surface tension decay). The droplet morphologies associated with each case are represented with the same color box. The droplet morphology at each time interval during the simulation is portrayed using the maximum density contours overlapped on the surface tension decay plot in Fig. 7. The conditions used for this analysis are as follows: the droplet diameter is 50 μm and the ratio of droplet density to nitrogen density calculated for nitrogen at 900 K and 6 MPa and *n*-dodecane at 363 K is 30. For this preliminary comparison, the droplet is impacted by a weak shockwave (Mach number equal to 1.01 corresponding to a post-shock gas velocity (U_g) equal to 10.4 m/s) to replicate a low Weber number equal to 6 for a constant surface tension coefficient of 20 mN/m represented by the blue line in Fig. 7. The flow speed imposed by the shock strength and thermodynamics conditions are kept constant for all the cases shown in Fig. 7. Analyzing the density contours for each case shows that for a constant surface tension, the droplet exhibits a vibrational mode where the droplet deforms from a circular shape and stretches in the spanwise direction before it regains its circular shape

with time. Neglecting the surface tension leads to a backward bag with a sheet-thinning regime. Increasing the rate of surface tension decay, i.e., reaching zero surface tension in a shorter time period during the simulations leads to no breakup. It is noted that the latest stage of break up for each case is different than the constant surface tension case and zero-surface tension case. This behavior shows that the droplet is undergoing less radial expansion at the initial stages due to the dominance of surface tension. The zero-surface tension case shows more lateral extension than any other case. The slower surface tension decay case follows the same trend. These results indicate that if surface tension decays during the period of droplet deformation, the resultant breakup morphologies can be different than the constant surface tension case. Therefore, to capture the behavior of transcritical aerobreakup, surface tension effects become important, particularly at lower Weber number regimes. However, accurately predicting the breakup modes is contingent on the surface tension decay rate. This emphasizes the need for a surface tension model as obtained from our MD results in Fig.3b, a pursuit that will be addressed in our forthcoming work.

D. Effects of Surface Tension Decay and Flow Speed

The effects of flow speed (U_g) and surface tension decay on droplet breakup morphologies at comparable non-dimensional time are shown in Fig. 8a-b. A 50 μm-diameter droplet at 363 K and an initial surface tension coefficient of σ_0 = 20 mN/m are considered in the simulations. The simulation conditions are the same as Spray A, i.e., 900 K and 6 MPa temperature and pressure for background nitrogen. Two different flow speeds are replicated by varying the shock strength. For each flow speed, the transient droplet morphology is shown for three surface tension behaviors: zero surface tension, represented with $We \rightarrow \infty$, decaying surface tension leading to Weber number variation ($5.7 < We < 120$ for lower flow speed and $23 < We < 500$ for higher flow speed), and constant surface tension associated with $We = 5$ and 23 for lower and higher flow speed, respectively.

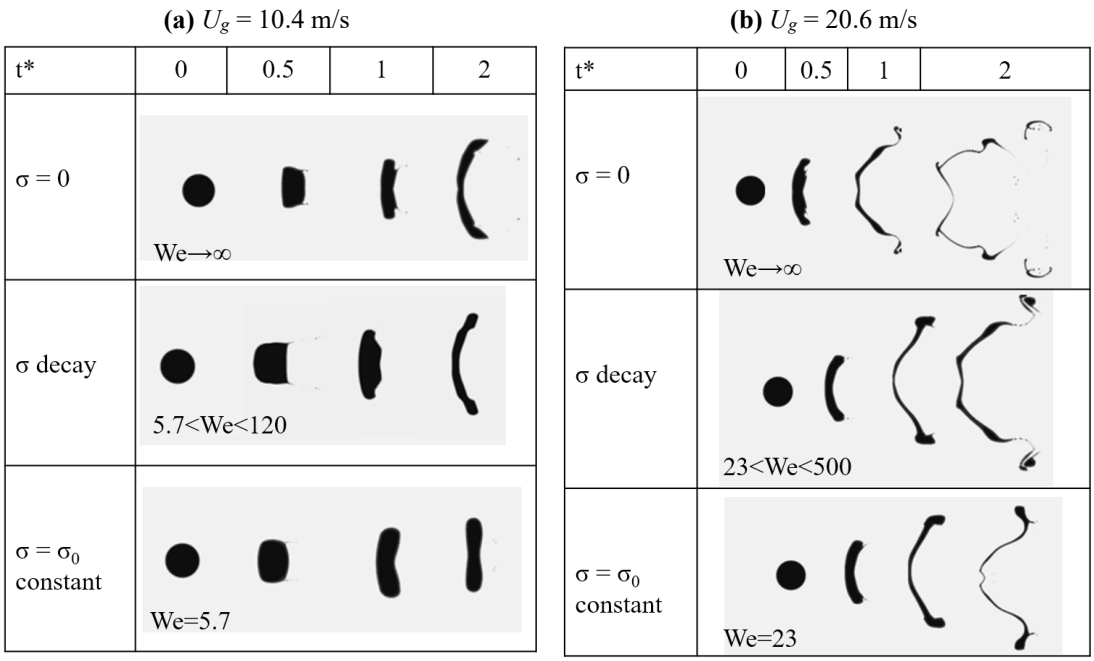

Figure 8. Different breakup morphologies for (a) M=1.01, U_g = 10.4 m/s ($5.7 < We < 120$) and (b) M=1.02, U_g = 20.6 m/s ($23 < We < 500$) at comparable non-dimensional times for Spray A conditions. The initial surface tension is σ_0 = 20 mN/m for both cases.

For lower flow speeds (Fig. 8a), the prevalence of surface tension effects limits the radial expansion of the droplet, preventing the formation of the crescent shape observed in the cases of zero surface tension and decaying surface tension. The droplet undergoes a bag breakup at zero surface tension and decaying surface tension; however, it exhibits a vibrational mode at constant surface tension as indicated in Fig. 8a. However, at higher flow speeds (Fig. 8b), the droplet deformation into a crescent shape with thin sheets occurs earlier in time and surface tension effects mainly influence the smallest structure in the thin-sheet regions at the wake of the droplet and near the radially expanded parts of the droplet. Another distinction between the cases in Fig.8b shows that the indentation seen on the backward bags increases by decreasing the surface tension leading to $23 < We < 500$ and further increase in bag indentation occurs at zero surface tension ($We \rightarrow \infty$) as the droplet exhibits less resistance to the deformation (piercing) of the gas flow into

the droplet. These preliminary results clearly show that surface tension variation during droplet breakup can potentially modify the droplet breakup behavior; however, further investigations are needed to identify the breakup timescales compared to the timescales at which surface tension decays to zero as the droplet undergoes transition from subcritical to supercritical conditions.

V. Conclusions and Future Work

A 2D-DNS approach is employed to investigate the droplet breakup modes at transcritical conditions as a function of governing non-dimensional parameters, i.e., Weber number and density ratio. Molecular dynamics simulations using LAMMPS provide essential insights into the surface tension decay of *n*-dodecane droplets under transcritical conditions. The results demonstrate the diverse breakup modes of transcritical droplets, revealing a range of behaviors influenced by the Weber number, density ratio, and shockwave strength. The breakup modes for transcritical droplets include vibrational, backward bag, backward bag with sheet thinning, sheet thinning, and whiplash with sheet thinning with an increase in *We*. The transcritical modes vary with both density ratio and Weber number. This is in contrast to subcritical breakup modes, which are mainly a function of Weber number at lower Ohnesorg numbers. This study systematically explores the effects of parameter space on the transcritical breakup modes, considering variations in ambient temperature and pressure for nitrogen, and variation in surface tension leading to temporal variation of the Weber number. Quantitative identification for the transcritical breakup modes is also developed using normal and transverse growth rates. The investigation into surface tension decay reveals that varying rates of decay lead to different breakup morphologies, emphasizing the importance of capturing the dynamic evolution of surface tension during droplet deformation. This work highlights the complexity of transcritical droplet breakup and the need for a comprehensive understanding of surface tension effects, especially at lower Weber number regimes (*We*: 1-100). It has been identified that calculating an accurate decay rate is necessary for understanding the appropriate breakup regime, which is supplied from the MD simulation. Additionally, the examination of flow speed and surface tension effects demonstrates their significant impact on droplet deformation and fragmentation. The presented findings underscore the need for further research to precisely model surface tension decay at transcritical conditions and to explore the timescales of breakup compared to surface tension variations. The results provide a foundation for future studies aiming to enhance our understanding of droplet behavior in transcritical environments, with potential applications in high-speed and high-pressure liquid-fuel systems and combustion processes.

Acknowledgements

This paper acknowledges the support received from the National Science Foundation under Grant No #2237124. The authors express their gratitude to the High-Performance Research Computing (HPRC) resources at Texas A&M University for providing the necessary computational infrastructure to conduct the simulations.

References

1. Zhong, F., et al., *Heat transfer of aviation kerosene at supercritical conditions.* Journal of Thermophysics and Heat Transfer, 2009. **23**(3): p. 543-550.
2. Sun, F., et al., *On assessment of heat transfer deterioration of a channel with supercritical n-decane for scramjet engines cooling.* International Journal of Heat and Mass Transfer, 2019. **135**: p. 782-795.
3. Jofre, L. and J. Urzay, *Transcritical diffuse-interface hydrodynamics of propellants in high-pressure combustors of chemical propulsion systems.* Progress in Energy and Combustion Science, 2021. **82**: p. 100877.
4. Williams, A., *Combustion of droplets of liquid fuels: A review.* Combustion and Flame, 1973. **21**(1): p. 1-31.
5. Tarifa, C., A. Crespo, and E. Fraga, *A theoretical model for the combustion of droplets in supercritical conditions and gas pockets.* Astronautica Acta, 1972. **17**.
6. Sirignano, W. and J.-P. Delplanque, *Transcritical vaporization of liquid fuels and propellants.* Journal of Propulsion and Power, 1999. **15**(6): p. 896-902.
7. Banuti, D.T., *Crossing the Widom-line – Supercritical pseudo-boiling.* The Journal of Supercritical Fluids, 2015. **98**: p. 12-16.
8. Mayer, W.O.H., et al., *Propellant Atomization and Ignition Phenomena in Liquid Oxygen/Gaseous Hydrogen Rocket Combustors.* Journal of Propulsion and Power, 2001. **17**(4): p. 794-799.
9. Dahms, R.N., et al., *Understanding high-pressure gas-liquid interface phenomena in Diesel engines.* Proceedings of the Combustion Institute, 2013. **34**(1): p. 1667-1675.
10. Klima, T.C. and A.S. Braeuer, *Vapor-liquid-equilibria of fuel-nitrogen systems at engine-like conditions measured with Raman spectroscopy in micro capillaries.* Fuel, 2019. **238**: p. 312-319.
11. Das, P. and H.S. Udaykumar, *A sharp-interface method for the simulation of shock-induced vaporization of droplets.* Journal of Computational Physics, 2020. **405**(109005).
12. Q. Wan, H.J., R. Deiterding, V. Eliasson, *Numerical and experimental investigation of oblique shock wave refection of a water wedge.* Jounal of Fluid Mechanics, 2017. **826**: p. 732-758.

13. Garrick, D.P., M. Owkes, and J.D. Regele, *A finite-volume HLLC-based scheme for compressible interfacial flows with surface tension.* Journal of Computational Physics, 2017. **339**: p. 46-67.
14. Meng, J.C. and T. Colonius, *Numerical simulations of the early stages of high-speed droplet breakup.* Shock Waves, 2015. **25**(4): p. 399-414.
15. Meng, J.C. and T. Colonius, *Numerical simulation of the aerobreakup of a water droplet.* Journal of Fluid Mechanics, 2018. **835**: p. 1108.
16. Garrick, D.P., W.A. Hagen, and J.D. Regele, *An interface capturing scheme for modeling atomization in compressible flows.* Journal of Computational Physics, 2017. **344**: p. 260-280.
17. Chen, C. and X. Jiang, *Transport property prediction and inhomogeneity analysis of supercritical n-Dodecane by molecular dynamics simulation.* Fuel, 2019. **244**: p. 48-60.
18. Wei, W., et al., *Large eddy simulation and proper orthogonal decomposition analysis of fuel injection under trans/supercritical conditions.* Computers & Fluids, 2019. **179**: p. 150-162.
19. Boyd, B. and D. Jarrahbashi, *Shock wave interaction with a transcritical fuel droplet.* International Conference on Liquid Atomization and Spray Systems (ICLASS), 2021. **1**.
20. Boggavarapu, P., et al., *Secondary breakup of water and surrogate fuels: Breakup modes and resultant droplet sizes.* International Journal of Multiphase Flow, 2021. **145**: p. 103816.
21. Nykteri, G. and M. Gavaises, *Droplet aerobreakup under the shear-induced entrainment regime using a multiscale two-fluid approach.* Physical Review Fluids, 2021. **6**(8): p. 084304.
22. Meng, J.C. and T. Colonius, *Numerical simulation of the aerobreakup of a water droplet.* Journal of Fluid Mechanics, 2018. **835**: p. 1108-1135.
23. Tudisco, P. and S. Menon, *Numerical Investigations of Phase-Separation During Multi-Component Mixing at Super-Critical Conditions.* Flow, Turbulence and Combustion, 2020. **104**(2): p. 693-724.
24. Boyd, B. and D. Jarrahbashi, *A diffuse-interface method for reducing spurious pressure oscillations in multicomponent transcritical flow simulations.* Computers & Fluids, 2021: p. 104924.
25. Ma, P.C., Y. Lv, and M. Ihme, *An entropy-stable hybrid scheme for simulations of transcritical real-fluid flows.* Journal of Computational Physics, 2017. **340**: p. 330-357.
26. Ma, P.C., et al., *Large-eddy simulations of transcritical injection and auto-ignition using diffuse-interface method and finite-rate chemistry.* Proceedings of the Combustion Institute, 2019. **37**(3): p. 3303-3310.
27. Matheis, J. and S. Hickel, *Multi-component vapor-liquid equilibrium model for LES of high-pressure fuel injection and application to ECN Spray A.* International Journal of Multiphase Flow, 2018. **99**: p. 294-311.
28. Ruiz, A.M., et al., *Numerical Benchmark for High-Reynolds-Number Supercritical Flows with Large Density Gradients.* AIAA Journal, 2015. **54**(5): p. 1445-1460.
29. Schmitt, T., et al., *Large-Eddy Simulation of Supercritical-Pressure Round Jets.* AIAA Journal, 2010. **48**(9): p. 2133-2144.
30. Matheis, J., et al., *Large-eddy simulation of cryogenic jet injection at supercritical pressures.* 2016.
31. Müller, H., et al., *Large-eddy simulation of nitrogen injection at trans-and supercritical conditions.* Physics of Fluids, 2016. **28**(1): p. 015102.
32. Oefelein, J., R. Dahms, and G. Lacaze, *Detailed modeling and simulation of high-pressure fuel injection processes in diesel engines.* SAE International Journal of Engines, 2012. **5**(3): p. 1410-1419.
33. Oefelein, J., et al., *Effects of real-fluid thermodynamics on high-pressure fuel injection processes.* SAE International Journal of Engines, 2014. **7**(3): p. 1125-1136.
34. Banuti, D.T., P.C. Ma, and M. Ihme. *Phase separation analysis in supercritical injection using large-eddy-simulation and vapor-liquid-equilibrium*. in *53rd AIAA/SAE/ASEE Joint Propulsion Conference*. 2017.
35. Okong'o, N. and J. Bellan, *Perturbation and initial Reynolds number effects on transition attainment of supercritical, binary, temporal mixing layers.* Computers & Fluids, 2004. **33**(8): p. 1023-1046.
36. Okong'o, N. and J. Bellan, *Small-scale dissipation in binary-species, thermodynamically supercritical, transitional mixing layers.* Computers & Fluids, 2010. **39**(7): p. 1112-1124.
37. Crua, C., J. Manin, and L.M. Pickett, *On the transcritical mixing of fuels at diesel engine conditions.* Fuel, 2017. **208**: p. 535-548.
38. Jangale, P., et al., *Surface tension and evaporation behavior of liquid fuel droplets at transcritical conditions: Towards bridging the gap between molecular dynamics and continuum simulations.* Fuel, 2024. **358**: p. 130187.
39. Jain, S.S., et al., *Secondary breakup of drops at moderate Weber numbers: Effect of Density ratio and Reynolds number.* International Journal of Multiphase Flow, 2019. **117**: p. 25-41.
40. Hinze, J.O., *Fundamentals of the hydrodynamic mechanism of splitting in dispersion processes.* AIChE journal, 1955. **1**(3): p. 289-295.
41. Krzeczkowski, S.A., *Measurement of liquid droplet disintegration mechanisms.* International Journal of multiphase flow, 1980. **6**(3): p. 227-239.
42. Chou, W.-H. and G. Faeth, *Temporal properties of secondary drop breakup in the bag breakup regime.* International journal of multiphase flow, 1998. **24**(6): p. 889-912.
43. Pilch, M. and C.A. Erdman, *Use of breakup time data and velocity history data to predict the maximum size of stable fragments for acceleration-induced breakup of a liquid drop.* International Journal of Multiphase Flow, 1987. **13**(6): p. 741-757.

44. Theofanous, T., et al., *Aerobreakup in disturbed subsonic and supersonic flow fields.* Journal of Fluid Mechanics, 2007. **593**: p. 131-170.
45. Theofanous, T.G. and G.J. Li, *On the physics of aerobreakup.* Physics of Fluids, 2008. **20**(5): p. 052103.
46. Boyd, B. and D. Jarrahbashi, *Numerical study of the transcritical shock-droplet interaction.* Physical Review Fluids, 2021. **6**(11): p. 113601.
47. Gottlieb, S. and C.-W. Shu, *Total variation diminishing Runge-Kutta schemes.* Mathematics of computation, 1998. **67**(221): p. 73-85.
48. Johnsen, E. and T. Colonius, *Implementation of WENO schemes in compressible multicomponent flow problems.* Journal of Computational Physics, 2006. **219**(2): p. 715-732.
49. Boyd, B. and S. Becker, *Numerical modelling of an acoustically-driven bubble collapse near a solid boundary.* Fluid Dynamics Research, 2018. **50**(6): p. 065506.
50. Boyd, B. and S. Becker, *Numerical modeling of the acoustically driven growth and collapse of a cavitation bubble near a wall.* Physics of Fluids, 2019. **31**(3): p. 032102.
51. Perigaud, G. and R. Saurel, *A compressible flow model with capillary effects.* Journal of Computational Physics, 2005. **209**(1): p. 139-178.
52. Thompson, A.P., et al., *LAMMPS - a flexible simulation tool for particle-based materials modeling at the atomic, meso, and continuum scales.* Computer Physics Communications, 2022. **271**: p. 108171.
53. Irving, J.H. and J.G. Kirkwood, *The Statistical Mechanical Theory of Transport Processes. IV. The Equations of Hydrodynamics.* The Journal of Chemical Physics, 1950. **18**(6): p. 817-829.
54. Bruneaux, G., et al., *Comparison of Diesel Spray Combustion in Different High-Temperature, High-Pressure Facilities.* SAE International Journal of Engines, 2010. **3**(2): p. 156-181.